Development of a cooled He*(2 3S) beam source for measurements of state-resolved collision energy dependence of Penning ionization cross sections: Evidence for a stereospecific attractive well around methyl group in CH3CN

著者	岸本 直樹

journal or publication title	Journal of chemical physics
volume	123
number	19
page range	194308-1-194308-13
year	2005
URL	http://hdl.handle.net/10097/35263

doi: 10.1063/1.2114808

Development of a cooled $He^*(2\,^3S)$ beam source for measurements of state-resolved collision energy dependence of Penning ionization cross sections: Evidence for a stereospecific attractive well around methyl group in CH_3CN

Takuya Horio, Masakazu Yamazaki, Satoshi Maeda, Takuro Hatamoto, Naoki Kishimoto, and Koichi Ohno[a)]
Department of Chemistry, Graduate School of Science, Tohoku University, Aramaki, Aoba-ku, Sendai 980-8578, Japan

(Received 1 August 2005; accepted 16 September 2005; published online 15 November 2005)

A low-temperature discharge nozzle source with a liquid-N_2 circulator for $He^*(2\,^3S)$ metastable atoms has been developed in order to obtain the state-resolved collision energy dependence of Penning ionization cross sections in a low collision energy range from 20 to 80 meV. By controlling the discharge condition, we have made it possible to measure the collision energy dependence of *partial* ionization cross sections (CEDPICS) for a well-studied system of $CH_3CN+He^*(2\,^3S)$ in a wide energy range from 20 to 350 meV. The anisotropic interaction potential energy surface for the present system was obtained starting from an *ab initio* model potential via an optimization procedure based on classical trajectory calculations for the observed CEDPICS. A dominant attractive well depth was found to be 423 meV (ca. 10 kcal/mol) at a distance of 3.20 Å from the center of mass of CH_3CN in the N-atom side along the CCN axis. In addition, a weak attractive well (ca. 0.9 kcal/mol) surrounding the methyl group ($-CH_3$) has been found and ascribed to the interaction between an unoccupied molecular orbital of CH_3CN and $2s$ atomic orbital of $He^*(2\,^3S)$. © *2005 American Institute of Physics*. [DOI: 10.1063/1.2114808]

I. INTRODUCTION

The reactions of electronically excited atoms with molecules have been of great importance in plasma physics and its applications. One of the most fundamental reaction processes involving long-lived metastable rare gas atoms is Penning ionization,[1] which occurs when a molecule M collides with a metastable rare gas atom A^* having an excitation energy larger than the ionization potential (IP) of M,

$$A^* + M \rightarrow M_i^+ + A + e^-. \tag{1}$$

The electron exchange model proposed by Hotop and Niehaus[2] characterizes this chemi-ionization process; an electron of a molecular orbital (MO) ϕ of M is transferred to the inner vacant orbital χ of A^*, and simultaneously an excited electron of A^* is ejected. Therefore, the reaction probability producing different ionic states of $M(M_i^+)$ depends on the mutual overlap between the MO ϕ to be ionized and the inner vacant orbital χ of A^*. Since the kinetic energy of the ejected electrons (E_e) depends on the respective ionization potentials $(\mathrm{IP})_i$ for corresponding ionic states of M_i^+, Penning ionization electron spectroscopy[3] has made it possible to obtain the kinetic-energy distribution of the ejected electrons, namely, partial ionization cross sections for each ionic state M_i^+.[3–5] Branching ratios for the production of M_i^+ estimated from relative band intensities in Penning ionization electron spectrum (PIES) can be related with the electron density outside the repulsive surface of the target molecule [exterior electron density (EED)].[6–8]

The collision energy (E_c) between A^* and M is another important variable in this process, since the ionization cross section is a function of the relative velocity between the colliding systems. From this standpoint, the collision energy dependence of *total* ionization cross sections $\sigma_T(E_c)$ for atomic and molecular targets has been studied extensively by detecting produced ions.[4,9–16] These studies have been performed in a considerably wide dynamical range in order to investigate the interaction potential $V^*(R)$ between A^* and M [e.g., the studied collision energy range is 0.003–6.0 eV for the systems of $He^*(2\,^{1,3}S)+$Ar, Kr, and Xe (Ref. 16); however, the collision energy dependence of *partial* ionization cross sections $\sigma_i(E_c)$ (CEDPICS) for the molecules with various ionic states of M_i^+ has been disregarded for a long time.

Since the spatial distribution of each MO in a target molecule is usually highly anisotropic, partial ionization cross sections for Penning ionization should have the information on collisional reactions in the spatially limited regions where the electron density of the corresponding MOs mainly distributes. Therefore, even though target molecules are randomly oriented, CEDPICS directly reflects not only the stereoreactivity of MOs to be ionized but also the anisotropic feature of the interaction potential energy surface. The CEDPICS for molecular targets was first observed by means of Penning ionization electron spectroscopic techniques combined with a time-of-flight (TOF) method for $He^*(2\,^3S)$

[a)]Author to whom correspondence should be addressed. FAX: +81-22-795-6580. Electronic mail: ohnok@qpcrkk.chem.tohoku.ac.jp

(excitation energy=19.82 eV) beam.[17–19] Velocity-controlled crossed supersonic molecular-beam techniques have been utilized to observe collision-energy-resolved PIES with stepwise selections of the well-defined collision energies.[20–23] In the last decade, collision-energy/electron-energy-resolved two-dimensional Penning ionization electron spectroscopy (2D-PIES) has been developed,[24] in which signals of the ejected electrons can be measured as functions of both E_e and E_c.

These experimental approaches based on an electron spectroscopic technique have provided straightforward studies on the anisotropy of the interaction potential energy surface between A^* and M. However, the studied dynamical energy range was considerably narrower than that in measurements of $\sigma_T(E_c)$. Especially in the low collision energy region corresponding to the thermal energies around a room temperature (ca. 38 meV), experimental studies for the collision energy dependence of σ_i have not been performed; previous collision energy ranges are 68–180 meV for $He^*(2\,^1S)+N_2$,[22] 60–120 meV for $He^*(2\,^{1,3}S)+N_2O$ (Ref. 23) in crossed supersonic molecular-beam studies, 60–400 meV for $He^*(2\,^{1,3}S)+Ar$,[24] 70–350 meV for $He^*(2\,^3S)+N_2$ (Ref. 25) in 2D-PIES studies, etc. This was mainly due to a considerable reduction of counting rates in electron signals caused by the weak intensity of low velocity metastable atomic beams. Therefore, it has been quite difficult to probe weak interactions (ca. 5–50 meV) between A^* and M. In order to evaluate anisotropic potential energy surfaces in good accuracy as well as to overcome the disadvantage of narrow dynamical range, experimental investigations of partial ionization cross sections σ_i at the lower collision energies need to be established.

Theoretical studies have also been performed extensively to understand collisional ionization dynamics. Nakamura[26] and Miller[27] established fundamental theories of Penning ionization, where both the ionization width and the interaction potentials for a colliding system were required to comprehend collisional ionization dynamics. These theories were applied to molecular targets with simple species such as H_2 (Refs. 28 and 29) and N_2.[30,31] For the system of $N_2+He^*(2\,^3S)$, the CEDPICS for N_2 was obtained by trajectory calculations based on an *ab initio* potential energy surface and ionization widths with various approximations.[30,31] Semiempirical approaches for the interaction potential energy surface have been employed for relatively large systems of $Ne^*(^3P_{0,2})+CH_3Cl$,[32] and very recently, for $He^*(2\,^{3,1}S), Ne^*(^3P_{0,2})+N_2O$.[33] In the latter work, *ab initio* investigations of the interaction potential energy surfaces for the excited states have also been made to verify their semiempirical calculations.[33]

Recent *ab initio* calculations have shown good agreement with the observed electron energy spectra as well as collision energy dependence of ionization cross sections in the case of atomic targets,[34,35] while it has been still a difficult problem to evaluate interaction potentials in good accuracy under *ab initio* treatments for molecular targets. This is due to difficulties in constructing highly anisotropic interaction potentials for A^*-M systems embedded in an ionization continuum. For calculating interaction potential energy surfaces, an alternative approach avoiding the difficulties in treating the highly excited states around 20 eV is to replace metastable rare gas atoms with the corresponding alkali atoms on the basis of the well-known resemblance in interactions with various atomic targets.[36–39] Ogawa and Ohno have reported classical trajectory calculations for $N_2+He^*(2\,^3S)$ based on an *ab initio* Li model potential and an overlap approximation for the ionization widths.[40] The calculation has well explained the observed features in CEDPICS;[40] however, optimization procedures for the observed CEDPICS were needed in order to obtain more quantitative intermolecular potential energy surface. Very recently, an overlap expansion method for improving *ab initio* Li model potentials has been proposed on the basis of the fact that intermolecular interactions are more or less related to overlaps of MOs concerned.[41] This method has been used to obtain interaction potential energy surfaces for N_2,[41] CO,[41] C_2H_2,[41,42] OCS,[42] and C_6H_6 (Ref. 43) $+He^*(2\,^3S)$. In the system of $CH_3CN+He^*(2\,^3S)$, classical trajectory calculations on an *ab initio* Li model potential showed fairly good agreement with the observed CEDPICS in the collision energies between 80 and 300 meV.[44] However, there has been disagreement between the observed CEDPICS and the calculated one for the ionic $B(^2E)$ state of CH_3CN^+ [corresponding MO is $1e(\sigma_{CH})$], especially in lower collision energies below 100 meV.[44]

In this work, we have developed a cooled $He^*(2\,^3S)$ beam source for the measurements of the state-resolved collision energy dependence of partial ionization cross sections at the collision energies less than 50 meV. The experimental details with the cooled discharge nozzle source and characteristics of the produced $He^*(2\,^3S)$ beams are reported. The present discharge nozzle source was also compared with the other cooled discharge nozzle sources that have been developed recently in the field of atomic quantum optics and physics. By means of the cooled discharge nozzle source, CEDPICS for the well-studied system of $CH_3CN+He^*(2\,^3S)$ (Refs. 44–46) has been measured in the collision energy range from 20 to 350 meV for the first time. In addition, the anisotropic interaction potential energy surface for the present system was obtained starting from an *ab initio* model potential via the above optimization procedure based on classical trajectory calculations for the observed CEDPICS. The present work is the first attempt to combine the new experimental studies by means of the cooled $He^*(2\,^3S)$ beam source with the optimization method of the interaction potential by the overlap expansion method. CEDPICS obtained at the lower collision energies would provide us a good test for evaluating such a highly anisotroipic interaction potential. The observed CEDPICS and the optimized interaction potential energy surface have been discussed in detail.

II. EXPERIMENT

Figure 1 shows a schematic view of the present apparatus with four differentially pumped chambers of (A)–(D), which is almost identical to the one reported previously[47] except for additions of a low-temperature discharge nozzle

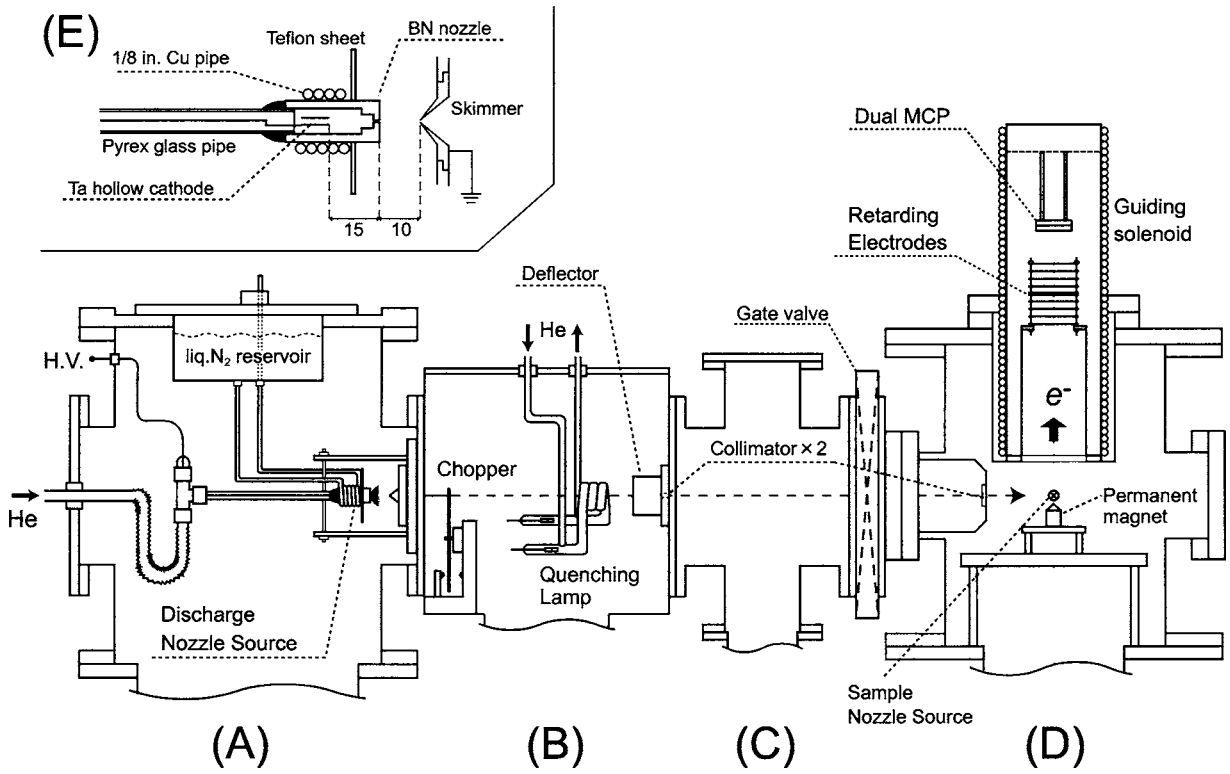

FIG. 1. Schematic view of the present apparatus with a low-temperature discharge nozzle source. (A) Metastable atom beam source with a liquid-N_2 circulator. (B) Beam-controlling chamber with a mechanical chopper, a quenching lamp, and a deflector. (C) Buffer chamber. (D) Reaction chamber with a magnetic bottle retarding-type electron-energy analyzer. (E) Detail of the cooled discharge nozzle source (geometrical size in millimeter).

source in the chamber (A) and the buffer chamber (C) for further differential pumping in order to improve vacuum in the reaction chamber (D). Although the outline of the apparatus has been reported previously,[48] a detailed description about the experimental methods with the cooled discharge nozzle source is given here.

The present dc discharge source has been developed on the basis of the high-intensity $He^*(2\,^3S)$ beam source.[18,19] The chamber (A) for the metastable atom beam source was pumped by a water-baffled 10 in. oil diffusion pump ($3700\ l\ s^{-1}$, effectively $2500\ l\ s^{-1}$ through the baffle) and a Roots pump ($70\ l\ s^{-1}$). Metastable atoms of $He^*(2\,^1S, 2\,^3S)$ were produced by a nozzle discharge between a tantalum hollow cathode [5 mm outer diameter (o.d.), 4.6 mm inner diameter (i.d), 25 mm length] inside a Pyrex glass pipe (10.4 mm o.d., 8.0 mm i.d.) and a stainless-steel conical skimmer (orifice diameter=0.7 mm). He gas (purity $>$ 99.999 95%) was introduced in the Pyrex glass tube connected with a stainless-steel flexible tube and another glass pipe. A machined piece of boron nitride (BN) cap (orifice diameter =0.8 mm) was attached onto the discharge region in the Pyrex glass pipe with a heat-resistant inorganic adhesive (Toagosei, ARON CERAMIC D, the main component is alumina). BN has been used because of its low electrical conductivity and good heat conductivity. The nozzle cap can be cooled by circulating liquid N_2 in a 1/8 in. copper pipe surrounding the BN nozzle cap for experiments at lower collision energies between 20 and 80 meV. A layer of aluminum foil is wedged between the BN cap and the 1/8 in. copper pipe for surface contact. The volume of the liquid-N_2 reservoir mounted on the top of the chamber (A) is *ca.* 2 l. In the lower collision-energy (20–80 meV) experiments, the nozzle discharge source was cooled by the liquid-N_2 circulator with typical discharge voltage and current of 330 V and 18 mA, respectively. In higher collision-energy (80–350 meV) experiments, the discharge voltage and current were typically 300 V and 45 mA, respectively, without the liquid-N_2 circulator. The stagnation pressure of He gas in the upper stream of the nozzle was 40 Torr. The typical pressure in the chamber (A) under the discharge of He^* beam was 2×10^{-4} Torr (base pressure=2×10^{-7} Torr).

In the chamber (B), which is pumped by a water-baffled 4 in. oil diffusion pump ($600\ l\ s^{-1}$, effectively $200\ l\ s^{-1}$ through the baffle), the metastable beams were pulsed using a mechanical chopper (100 mm diameter, 0.2 mm thick) with a slit width of 2 mm rotating between 240 and 320 Hz for TOF measurements. This mechanical chopper was rotated using a synchronous motor (Globe Motors: 18A1003-2) with a sine/cosine wave oscillator. A light-emitting diode and a photodiode were used to produce the starting origin of the TOF measurements. The $He^*(2\,^1S)$ component was quenched by a water-cooled He discharge lamp (discharge current and voltage: 35 mA and 900 V). The typical pressure in the chamber (B) under the operation of the nozzle discharge was 8×10^{-6} Torr (base pressure=8×10^{-7} Torr). The metastable atomic beam of $He^*(2\,^3S)$ component went through the buffer chamber (C) for differential pumping and beam collimation [the pressure is typically 5×10^{-7} Torr with the $He^*(2\,^3S)$ beam loaded], then it was introduced into the reaction chamber (D), where gaseous samples from an

effusive beam source (orifice diameter=1.5 mm) were prepared at room temperature. CH_3CN (purity>99.7%) was commercially purchased and purified by several freeze-pump-thawed cycles.

The kinetic-energy (E_e) distribution of the ejected electrons was observed by means of an electrostatic retarding-field-type analyzer equipped with an electron flight tube. The "magnetic bottle effect"[49–51] utilizing an inhomogeneous magnetic field with a permanent magnet and a guiding solenoid was also employed for high efficient measurements. Magnetic fields at the ionization region and in the electron flight tube were ca. 80 and 1.4 mT, respectively. Almost all the electrons were introduced into the series of retarding electrodes, and then passed electrons were detected by a dual microchannel plate (MCP, Hamamatsu F1552-21S) placed at the end of the flight tube. The base pressure in the reaction chamber (D) was 3×10^{-8} Torr, and measurements were carried out under the pressure of 1.4×10^{-6} Torr with both beams on.

In the state-resolved measurements of the collision energy dependence of Penning ionization cross sections, electron signals $I_e(E_e,t)$ as functions of electron kinetic energy (E_e) and TOF of the metastable $He^*(2\,^3S)$ atoms between the collision center and the chopper disk (flight length =735 mm) have been accumulated in a two-parameter multichannel scaler equipped with a retarding voltage generator (Laboratory Equipment Corporation, VSCANMCS NT-2400M) at a typical time resolution of 2 μs, a step of electron-energy scan of 40 meV, and a dwell time of 100 ms. The $I_e(E_e,t)$ can be converted to $I_e(E_e,v_{He^*})$ as functions of E_e and velocity of metastable $He^*(2\,^3S)$ atoms (v_{He^*}). The two-dimensional Penning ionization cross section $\sigma(E_e,v_r)$ with normalization by the velocity distribution of He^* atoms $I_{He^*}(v_{He^*})$ was obtained by the following equations:

$$\sigma(E_e,v_r)=c\frac{I_e(E_e,v_{He^*})}{I_{He^*}(v_{He^*})}\frac{v_{He^*}}{v_r}, \tag{2}$$

$$v_r=\sqrt{v_{He^*}^2+v_M^2}, \tag{3}$$

where c is a constant, v_r is the relative velocity between the $He^*(2\,^3S)$ atom and the target molecule, and v_M is the velocity of the target molecule, which is denoted by the following equation:

$$v_M=\sqrt{\frac{3k_BT}{m_M}}, \tag{4}$$

where k_B is the Boltzmann constant, T is the temperature of the effusive sample nozzle, and m_M is the mass of the target molecule. The velocity distribution $I_{He^*}(v_{He^*})$ was obtained from the TOF spectra of $He^*(2\,^3S)$ atoms measured by detecting secondary electrons emitted from an inserted stainless-steel needle. This needle can be moved through a rotary manipulator mounted on the reaction chamber (D). It should be noted that TOF of the ejected electrons to reach the electron detector (MCP) from the ionization region (<0.5 μs) can be negligible in comparison with that of the metastable $He^*(2\,^3S)$ atoms to reach the collision center from the chopper disk (200–800 μs). According to the equations above, $\sigma(E_e,v_r)$ is converted to the final form $\sigma(E_e,E_c)$ with the reduced mass of the colliding system μ:

$$E_c=\frac{1}{2}\mu v_r^2. \tag{5}$$

III. CALCULATIONS

In order to discuss collisional ionization dynamics in detail and to investigate the anisotropic interaction potential energy surface for the present system, CEDPICS has been theoretically constructed. Since a full description about the present methods of theoretical calculations has been reported previously,[41,44] only the outline is given here. First we started from calculating an approximate interaction potential energy surface V_0 using $Li(2\,^2S)$ in place of $He^*(2\,^3S)$ on the basis of the well-known resemblance between $He^*(2\,^3S)$ and $Li(2\,^2S)$ (Refs. 36–39) (V_0:Li model potential), as mentioned in Sec. I. The Li model potential V_0 can be expressed as functions of R,θ and ϕ, where R is the distance between the $Li(2\,^2S)$ atom and the center of mass of CH_3CN, θ is the polar angle from the C_{3v} axis (CCN axis), and ϕ is the azimuthal angle, respectively. Interaction potential energy surface $V_0(R,\theta,\phi)$ was calculated at 580 points for different orientations of CH_3CN with respect to $Li(2\,^2S)$ using the second-order Møller-Plesset perturbation theory with 6-31++G^{**} basis set. The basis-set superposition error (BSSE) was corrected by the full counterpoise method.[52] These calculations were performed with GAUSSIAN programs.[53]

Although $Li(2\,^2S)$ has the same valence electronic configuration as $He^*(2\,^3S)$ with a $2s$ electron which predominantly contributes to intermolecular interactions, it is natural that orbital interactions between $Li(2\,^2S)$ and target molecules should differ to some extent from those of $He^*(2\,^3S)$. Thus, in order to evaluate the anisotropic interaction more quantitatively, the interaction potential energy surface should be optimized to reproduce experimental observations of partial ionization cross sections as a function of collision energy E_c. In the present study, the overlap expansion method for improving *ab initio* model potentials[41] was employed for an optimization procedure. In this method, the model potential $V_{OE}(R,\theta,\phi)$ for correcting $V_0(R,\theta,\phi)$ is expressed by the following equations:

$$V_{OE}(R,\theta,\phi)=V_0(R,\theta,\phi)-\sum_i C_i|\langle\phi_i|\chi\rangle|^2, \tag{6}$$

$$\chi=\sqrt{\zeta^3/\pi}\exp[-\zeta r]. \tag{7}$$

Here, χ is a normalized Slater-type s orbital function with an exponent ζ, which is located at the position of the He^*/Li atom. r is the distance from the center of χ. This correction method has been designed to describe effectively anisotropic interactions by expanded terms using overlap integrals between target MOs ϕ_i concerned and an atomic orbital χ. The atomic-orbital exponent ζ and the expansion coefficients C_i are parameters to be optimized. In trial calculations, it was found that the following MOs ϕ_i should be selected in the correction term in Eq. (6); occupied orbitals of $6a_1,1e,7a_1$, and $2e$(HOMO) (highest occupied molecular orbital) and un-

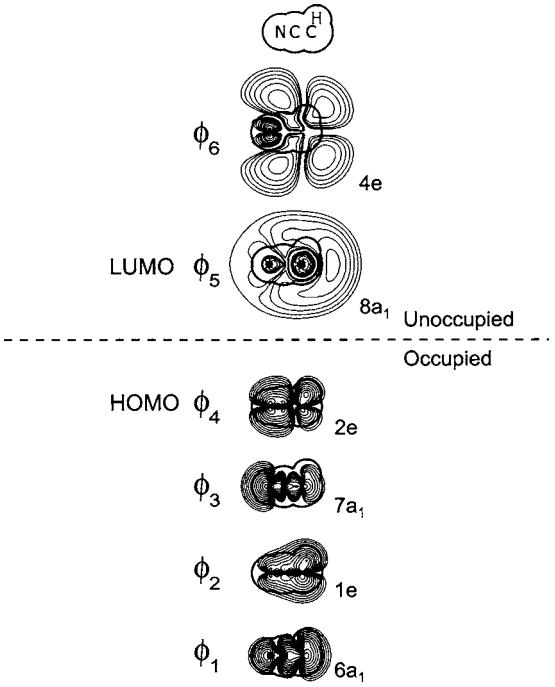

FIG. 2. Contour maps of electron density distribution of MOs of CH_3CN. Occupied MOs ($6a_1, 1e, 7a_1$, and $2e$) and unoccupied MOs ($8a_1$ and $4e$) were used for optimizations of potential energy surface (see Sec. III). The thick solid line in the contour maps represents the molecular surface of CH_3CN estimated approximately from van der Waals radii of component atoms in order to show the molecular shape schematically.

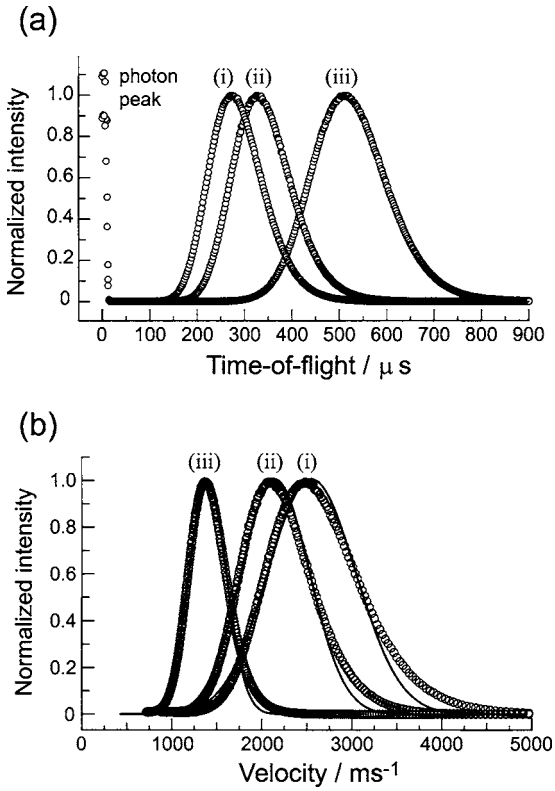

FIG. 3. (a) Typical time-of-flight (TOF) spectra for $He^*(2\,^3S)$ metastable atoms in discharge conditions of (i)–(iii) (see Table I). (b) The corresponding velocity distributions in discharge conditions of (i)–(iii). Observed data are plotted with circles. The fitted curves for the observed velocity distributions by Eq. (9) are shown with solid lines.

occupied orbitals of $8a_1$(LUMO) (lowest occupied molecular orbital) and $4e$ for CH_3CN. Electron density contour maps of respective MOs with the numbering of ϕ_i and C_i used in this work are listed in Fig. 2, where the thick solid line in the contour maps represents the molecular surface estimated approximately from van der Waals radii of component atoms in order to show the molecular shape schematically.

Classical trajectory calculations for obtaining theoretical CEDPICS of CH_3CN were made on the three-dimensional potential energy surface $V_0(R,\theta,\phi)$ or $V_{OE}(R,\theta,\phi)$. The relative motion of the colliding system was determined by solving the equation of motion. The molecular structure of CH_3CN was fixed at the experimental geometry. Since we found that the calculated equilibrium structure of the CH_3CN–Li complex was only slightly deformed from a single CH_3CN framework within ca. 0.01 Å,[54] the approximation of the frozen molecular structure is considered to be reasonable in the present trajectory calculations.

Calculations of 10 000 trajectories with randomly generated initial conditions (such as impact parameters, molecular orientation, and angular momenta) were performed for a given collision energy. The ionization width resulting in relative ionization cross section of each ionic state $\Gamma^{(i)}$ was evaluated on the basis of the following considerations; $\Gamma^{(i)}$ is mainly governed by the mutual overlap between the He $1s$ orbital (ψ_{1s}) and corresponding MOs (ϕ_i) to be ionized, and therefore, $\Gamma^{(i)}$ can be represented by

$$\Gamma^{(i)} = K^{(i)}|\langle\phi_i|\psi_{1s}\rangle|^2, \tag{8}$$

where $K^{(i)}$ is a constant value for each ionic state to be determined relatively in order to reproduce observed ionization branching ratio and collision energy dependence. Using this treatment, one can avoid theoretical and computational difficulties associated with direct calculations of the matrix elements including highly excited states for too many geometrical configurations.

Orbital functions ϕ_i and ψ_{1s} were obtained from *ab initio* self-consistent-field (SCF) calculations for the neutral molecule and a He atom with the same basis set as used in the Li model potential calculations. Parameters of C_i, ζ, and $K^{(i)}$ in Eqs. (6)–(8) were optimized by a nonlinear least-square-fitting method for the calculated CEDPICS in order to reproduce the observed one. The total calculated points for the collision energy E_c were 15, 20, 35, 50, 75, 100, 125, 150, 200, 250, 300, 400, and 500 meV. These points were selected by taking account of the estimated resolutions of the collision energy $E_c(\Delta E_c/E_c)$ in the present experiments [33% at E_c=20 meV (17–23 meV), 18% at E_c=50 meV (45–55 meV), 16% at E_c=100 meV (92–108 meV), and 20% at E_c =300 meV (270–330 meV)].

IV. RESULTS AND DISCUSSION

A. Velocity distributions of $He^*(2\,^3S)$ beams and characterization

Figures 3(a) and 3(b) show the observed TOF spectra and velocity distributions for $He^*(2\,^3S)$ metastable atoms in discharge conditions of (i)–(iii), which are plotted with

TABLE I. Discharge conditions and characteristics of $He^*(2\,^3S)$ metastable atom beams.

	Discharge condition				Beam property			
No.	P_d (W)[a]	P_0 (Torr)[a]	T_0 (K)[a]	Liquid N_2	T_s (K)[b]	v_s (ms^{-1})[b]	M[b]	I (10^{14} at. s^{-1} sr^{-1})[b]
(i)	13	40	610	off	128	2240	3.4	10
(ii)	6	40	430	off	76	1930	3.8	4.3
(iii)	6	40	180	on	22	1300	4.7	3.8

[a] P_d, P_0, and T_0 are the discharge power, the nozzle stagnation pressure, and the nozzle stagnation temperature, respectively.
[b] T_s, v_s, M, and I are the stream temperature, the stream velocity, the Mach number [Eqs. (9)–(11) in text], and the beam intensity, respectively. The parameters of T_s, v_s, and M were obtained by a best fit of the observed velocity distribution data by the use of Eq. (9).

circles. The discharge conditions of (i)–(iii) are summarized in Table I. The TOF signal having a peak at 0 μs in Fig. 3(a) was attributed to He I resonance photons (21.22 eV) from the discharge source.

In order to characterize the present $He^*(2\,^3S)$ beams, we have analyzed the observed velocity distributions by using the shifted Maxwellian velocity distribution $I(v)$:[55]

$$I(v) = Nv^3 \exp\left[-\frac{m}{2k_B T_s}(v - v_s)^2\right]. \quad (9)$$

Here, N is a normalization constant, m is the mass of helium atom, v_s is the stream velocity, and T_s is the stream temperature, respectively. v_s and T_s are the fitting parameters for the observed velocity distribution. In short, v_s is approximately equal to the most probable velocity in the beam, and T_s is related to the width of the velocity distribution. Using these two parameters v_s and T_s, the Mach number M, which is also used to characterize the nozzle beam, is expressed as follows:

$$M = v_s \sqrt{\frac{m}{\gamma k_B T_s}}, \quad (10)$$

where γ is the specific-heat ratio of the beam molecules (5/3 for monoatomic gases). T_s is also connected with the nozzle stagnation temperature T_0 by using the Mach number M and γ:

$$T_s = T_0\left(1 + \frac{\gamma - 1}{2}M^2\right)^{-1}. \quad (11)$$

Fitted curves for the observed velocity distributions of $He^*(2\,^3S)$ atoms in the discharge conditions of (i)–(iii) are shown with solid lines in Fig. 3(b). The obtained beam parameters are summarized in Table I. As can be seen in Fig. 3(b) and Table I, the liquid-N_2-cooled discharge nozzle source with the discharge power of 6 W makes it possible to produce low velocity $He^*(2\,^3S)$ metastable atoms (the mean velocity is ~1300 m/s). It should be noted that the nozzle discharge between the tantalum hollow cathode and the conical skimmer was not sustained below the discharge power of 3 W for the nozzle configuration shown in Fig. 1. The obtained Mach number M (3–5) indicates that the present nozzle source has operated under moderate supersonic molecular-beam conditions. The present beam characteristics are further discussed in Sec. IV B.

In order to check the validity of the present experimental method using the cooled discharge nozzle source, we measured the collision energy dependence of the total ionization cross section $\sigma_T(E_c)$ for $N_2 + He^*(2\,^3S)$ system. This measurement also enables us to check the performance of the present method in obtaining CEDPICS for molecular targets with various ionic states. In Fig. 4, the $\sigma_T(E_c)$ in the present work is compared with those measured by Illenberger and Niehaus[10] and Parr *et al.*,[14] who obtained the $\sigma_T(E_c)$ through the produced cation counts. All data for $\sigma_T(E_c)$ were normalized at E_c=90 meV. The observed CEDPICS for $N_2 + He^*(2\,^3S)$ [produced ionic states are $X(^2\Sigma_g^+), A(^2\Pi_u)$, and $B(^2\Sigma_u^+)$, respectively] is also shown in Fig. 4. Judging from the comparison of $\sigma_T(E_c)$, the present observed result is in good agreement with the earlier one in the studied collision energy range from 20 to 350 meV. In addition, it is found that CEDPICS can be measured in the same collision energy range, even in the case that ionization cross-section value is lowered by one order of magnitude with the decrease of collision energy, as can be seen in Fig. 4. This is mainly due to the use of the highly sensitive electron spectrometer equipped with magnetic bottle.

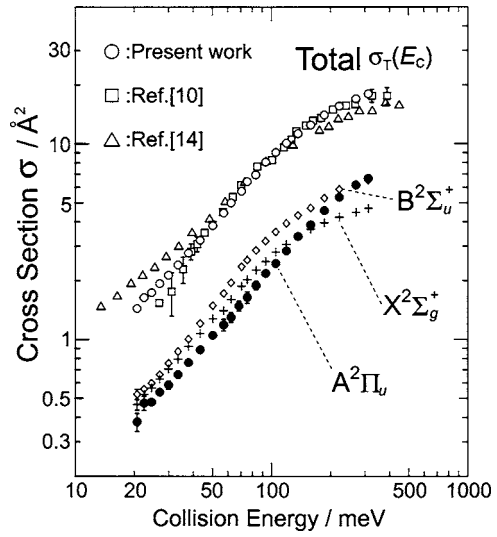

FIG. 4. Collision energy dependence of the total ionization cross section $\sigma_T(E_c)$ for $N_2 + He^*(2\,^3S)$ in the present work (open circles), Ref. 10 (squares), and Ref. 14 (triangles), respectively. All data for $\sigma_T(E_c)$ were normalized at E_c=90 meV. Collision energy dependence of the partial ionization cross sections (CEDPICS) for the produced ionic states of $X(^2\Sigma_g^+), A(^2\Pi_u)$, and $B(^2\Sigma_u^+)$ observed in this study is also shown.

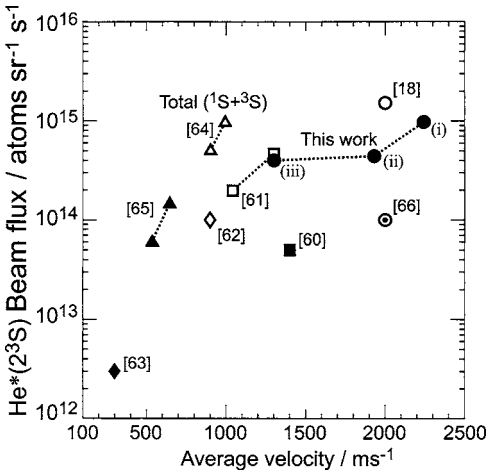

FIG. 5. Beam flux vs average velocities of $He^*(2\,^3S)$ metastable atomic beams in the present beam source [filled circles: the numbers of (i)–(iii) correspond to the discharge conditions in Table I] and in various beam sources reported in the numbered references (Refs. 18 and 60–66). The range of the average velocity of $He^*(2\,^3S)$ metastable atomic beam in each beam sources is shown with dotted lines.

B. Comparison of the present cooled discharge source with the others

Recently, helium metastable atomic beams have received much attention in many applications, such as atomic beam lithography[56,57] and atomic quantum optics [Bose-Einstein condensation (BEC),[58] photoassociation spectroscopy,[59] etc.]. In connection with these studies, various kinds of beam sources for cooled helium metastable atoms have been constructed extensively.[60–66] Here, we compare the present liquid-N_2-cooled discharge nozzle source with the other sources.

Figure 5 shows the beam flux versus the average velocity for $He^*(2\,^3S)$ metastable atomic beam. Generally, the beam flux decreases with the decrease of the average velocity. The present cooled beam source with a liquid-N_2 circulator can be well compared with the other sources. In all beam sources, nozzle discharge for helium gases has been employed, because a high-flux metastable beam ($>10^{14}$ at. $sr^{-1}\,s^{-1}$) can be obtained in nozzle-discharge-type sources, as reported previously.[18,67] Since nozzle discharge needs typically high currents (3–60 mA) in order to maintain the discharge, the nozzle temperature usually tends to be high. Thus, appropriate coolants, such as a liquid N_2,[60–62,64] or liquid He (Refs. 63 and 65) for the nozzle head or holder, are necessary to produce low velocity $He^*(2\,^3S)$ beams (<2000 m/s). The nozzle stagnation pressure P_0 and the diameter of the nozzle orifice are also important factors to affect the velocity distribution of $He^*(2\,^3S)$ beams. It is well known that a supersonic flow increases the velocity of atoms and molecules along the beam axis;[68] therefore, the nozzle source is desired to operate near the effusive flow regime in order to decrease the beam velocity as low as possible. Of course this causes the reduction of the beam intensity, thus, by taking this situation and the stability of the electric discharge into consideration, the conditions (such as stagnation pressure, diameter of the nozzle hole, and length between a cathode and an anode) should be optimized.

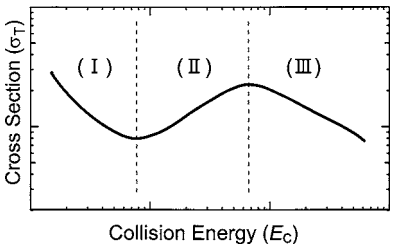

FIG. 6. Schematic illustration of the collision energy dependence of the total ionization cross section $\sigma_T(E_c)$ in $\log \sigma_T$-$\log E_c$ plots. A typical curve is divided into three regions; I, II, and III.

It should be noted that considerably low velocity $He^*(2\,^3S)$ beams (the average velocity is 300–600 m/s have been obtained by Woestenenk *et al.*[63] and Swansson *et al.*[65] Their discharge sources have operated at very low pressures (10^{-3}–10^{-1} Torr) and low discharge powers. Although the average velocity in this work is higher than that obtained in the above studies, the present cooled beam source is concluded to be satisfactory for the measurements of the state-resolved collision energy dependence of Penning ionization cross sections from the following reasons: (1) The fluctuation of the velocity distributions during measurements (this is a critical problem in experiments) is almost negligible, (2) the lifetime is fairly long (more than 300 h), and (3) studied collision energy range can be tuned without any geometrical changes of the nozzle discharge source [the average velocity range (1300–2300 m/s) is relatively wide, as can be seen in Fig. 5, where (i)–(iii) denote the discharge conditions in Table I].

C. General remarks on CEDPICS

Here, in order to discuss the observed CEDPICS for $CH_3CN+He^*(2\,^3S)$ system, the characteristic features of the collision energy dependence of Penning ionization cross sections should be introduced. For the system of $Ar+He^*(2\,^3S,2\,^1S)$, Olson[69] showed that the experimental features of the collision energy dependence of the total ionization cross sections $\sigma_T(E_c)$ were well reproduced by semi-empirical calculations based on the theory developed by Miller.[27] Figure 6 illustrates the general features of $\sigma_T(E_c)$, which can be summarized as follows. The first region (I) in Fig. 6 is related to the attractive potential well of the interaction potential $V^*(R)$, where R is a radial distance. In the case that the long-range attractive part of $V^*(R)$ plays a dominant role and its function form is the type of

$$V^*(R) \propto R^{-s}, \tag{12}$$

$\sigma_T(E_c)$ can be expressed by[4,10,18]

$$\sigma_T(E_c) \propto E_c^{-2/s}. \tag{13}$$

In the second region (II) in Fig. 6, the repulsive part of $V^*(R)$ governs $\sigma_T(E_c)$. Based on the assumption of simple analytical forms for $V^*(R)$ and the transition probability $W(R)$,

$$V^*(R) = B\exp(-dR) \tag{14}$$

and

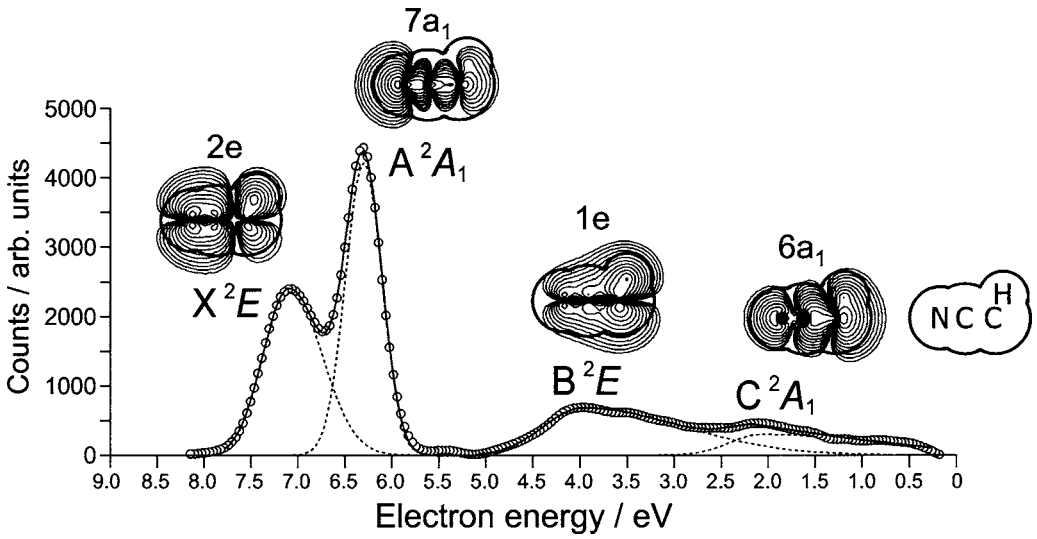

FIG. 7. Penning ionization electron spectrum (PIES) at a collision energy of 150 meV. Observed data are plotted with circles. Deconvoluted bands with asymmetric Gaussian functions and a fitted spectrum are drawn with dotted lines and a solid line, respectively. The calculated electron density contour maps of SCF-MOs corresponding to the respective ionic states are also shown.

$$W(R) = C \exp(-bR), \tag{15}$$

$\sigma_T(E_c)$ can be expressed by[4,10]

$$\sigma_T(E_c) \propto [\ln(B/E_c)^2](E_c/B)^{(b/d)-(1/2)}. \tag{16}$$

When the minor dependence of the first factor in Eq. (16) is neglected, the positive slope parameter m in the $\log \sigma - \log E_c$ plots can be related to the two parameters d and b in Eqs. (14) and (15):

$$m = (b/d) - (1/2), \tag{17}$$

where d is the effective steepness of the repulsive potential in $V^*(R)$, and b is the effective decay parameter of $W(R)$. As pointed out previously,[18] the effective parameter b in $W(R)$ can be related to the first ionization potential of the target molecule $M[\mathrm{IP}(M)]$,[70,71] and expressed by

$$b = 2[\mathrm{IP}(M)]^{1/2}. \tag{18}$$

It should be noted here that the value of b is common for all ionic states of a given target molecule. Thus, in the case of CEDPICS the positive slope parameter m can be connected with the repulsive interaction in the region where the electron density of the corresponding MO mainly distributes.[18] The third region (III) in Fig. 6 corresponds to the "hard-core collision" regime in Eq. (16); the parameter d becomes very large, and then b/d can be neglected in Eq. (16). Therefore, $\sigma_T(E_c)$ becomes proportional to $E_c^{-1/2}$. In this limit the effective interaction time governs the ionization cross section, however, the third region (III) is not included in the present measurements, since saturation of the ionization cross sections has not been observed.

D. CEDPICS and anisotropic interaction potential for $CH_3CN+He^*(2\,^3S)$

By collision with $He^*(2\,^3S)$ metastable atoms (excitation energy=19.82 eV), ionic states of $X(^2E)$,A(A12),B(E2), and $C(^2A_1)$ of CH_3CN^+ can be produced energetically. Figure 7 shows the observed PIES at the collision energy of 150 meV. Relative partial ionization cross sections were obtained by decomposition of the PIES into asymmetric Gaussian functions. In Fig. 7, a fitted spectrum and deconvoluted respective bands are also shown with a solid line and broken lines, respectively. From a comparison with the observed ultraviolet photoelectron spectrum (UPS) of CH_3CN,[72,73] these ionic states correspond to the removal of an electron from the $2e(\pi_{CN})$, $7a_1(n_N)$, $1e(\sigma_{CH})$, and $6a_1(\sigma_{CC})$ MOs, respectively. It should be noted that the produced ionic states can be classified into two classes of ^2E and $^2A_1$ according to the orbital symmetries of e and a_1 to be ionized. The calculated electron density contour maps of SCF-MOs corresponding to the respective ionic states are also shown in Fig. 7.

In Fig. 8, the observed $\log \sigma$(cross section) $-\log E_c$(collision energy) plots of CEDPICS for CH_3CN in the collision energy range of 20–350 meV are shown with circles. Since our experiments cannot provide an absolute

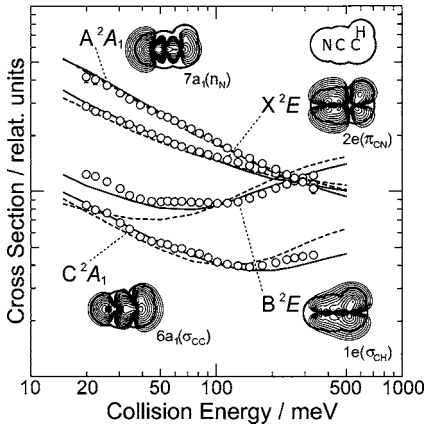

FIG. 8. Observed $\log \sigma$ (cross section)-$\log E_c$(collision energy) plots of CEDPICS for CH_3CN are shown with circles in the collision energy range from 20 to 350 meV. Calculated CEDPICSs obtained by the classical trajectory calculations utilizing the Li model potential energy surface V_0 (broken lines) and the optimized potential energy surface V_{OE} (solid lines) are also drawn.

TABLE II. Slope parameters m of CEDPICS for the $CH_3CN+He^*(2^3S)$ system in the collision energy range from 20 to 330 meV.

			m		
Ionic State	Orbital	Character	20–50 meV Obs. (Calc.)[a]	50–100 meV Obs. (Calc.)[a]	100–330 meV Obs. (Calc.)[a]
$X(^2E)$	$2e$	π_{CN}	−0.41(−0.47)	−0.34(−0.41)	−0.29(−0.27)
$A(^2A_1)$	$7a_1$	n_N	−0.54(−0.58)	−0.50(−0.54)	−0.47(−0.47)
$B(^2E)$	$1e$	σ_{CH}	−0.41(−0.30)	−0.03(0.03)	0.32 (0.35)
					−0.16(−0.25)/100–150
$C(^2A_1)$	$6a_1$	σ_{CC}	−0.54(−0.53)	−0.32(−0.37)	
					0.20(0.11)/150–330

[a]Slope parameters obtained by classical trajectory calculations on the optimized potential energy surface.

value of total ionization cross section, the vertical axis in Fig. 8 represents relative cross sections. It should be noted that experimental data for CH_3CN at lower collision energies between 20 and 80 meV have been obtained for the first time. In addition, observed data in a higher collision energy region from 80 to 350 meV have been refined by the present measurements with a high efficient electron spectrometer. Experimental statistical errors in the observed CEDPICS were found to be as large as the size of the plotted circles in Fig. 8 except for the edge of the low collision energy side. Figure 8 also compares the observed partial ionization cross sections as a function of collision energy E_c with those obtained by classical trajectory calculations utilizing the $V_0(R,\theta,\phi)$ (broken lines) or $V_{OE}(R,\theta,\phi)$ (solid lines) potential energy surfaces. As can be seen from the comparison of the observed CEDPICS with the calculated one in Fig. 8, the present trajectory calculations using the optimized potential energy surface V_{OE} well described the observed features of CEDPICS in the whole collision energy region of 20–350 meV. This indicates that the present theoretical treatments are considered to be sufficient so as to understand collisional ionization dynamics of $CH_3CN+He^*(2\,^3S)$ system in the studied collision energy range.

The observed slope parameters m for $\log\sigma$ vs $\log E_c$ plots for three collision energy regions of 20–50, 50–100, and 100–330 meV, which were obtained by a least-squares method, are summarized in Table II. The slope parameters m in the CEDPICS obtained by classical trajectory calculations on the $V_{OE}(R,\theta,\phi)$ potential energy surface are also listed in Table II. From Table II and Fig. 8, the negative collision energy dependence of partial ionization cross sections for $X(^2E)$ and $A(^2A_1)$ ionic states can be seen in the whole collision energy region of 20–350 meV. These observations indicate that the collisional ionizations into $X(^2E)$ and $A(^2A_1)$ states are governed by attractive potential throughout the studied collision energy range, namely, these correspond to the region (I) in Fig. 6; for an attractive interaction between the target molecule and a $He^*(2\,^3S)$ atom, a slower He^* atom can reach the reactive region over the centrifugal barrier than a faster He^* atom, which results in a large ionization cross section in the lower collision energies. In this case, trajectories passing through the attractive well region with large impact parameters predominantly contribute the enhancement of ionization cross sections in the lower collision energies.

Since Penning ionization processes crucially depend on local characteristics of electron distributions of target MOs, the large negative value of the slope parameter m for $A(^2A_1)$ ionic state [$m=-0.54$ (E_c: 20–50 meV), −0.50 (E_c: 50–100 meV), and −0.47 (E_c: 100–330 meV) in the observed CEDPICS] can be related to the strong attractive interaction around the N-atom side of CN group, where the electron distribution of the corresponding MO of $7a_1(n_N)$ mainly extends. Figures 9 and 10 show interaction potential energy curves for several configurations between Li (He^*) and CH_3CN, and a contour map of the optimized potential energy surface $V_{OE}(R,\theta,\phi)$, respectively. In Fig. 9, the optimized potential energy curves of V_{OE} and the Li model potential energy curves of V_0 are shown with solid lines (filled symbols) and broken lines (open symbols), respectively. In the contour map of $V_{OE}(R,\theta,\phi)$ in Fig. 10, the energy spacing of the contour lines for negative values is 50 meV for the energy range from −400 to −50 meV, and 5 meV for the energy range from −50 to 0 meV, respectively. In the case of positive values, the energy spacing is 100 meV. The contour map is taken in the σ_v vertical plane, which includes one of the

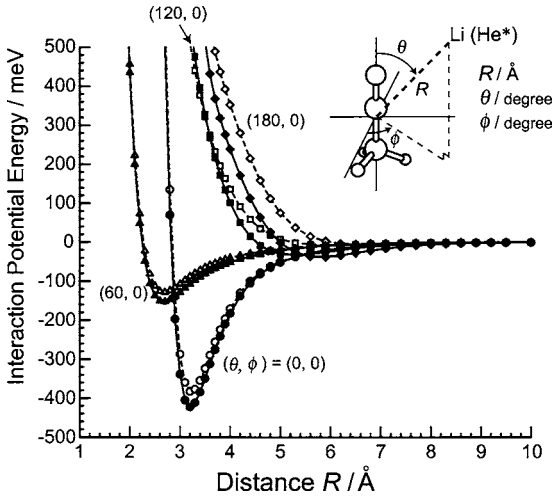

FIG. 9. Optimized interaction potential energy curves of V_{OE} (solid lines-filled symbols) and Li model interaction potential energy curves of V_0 (broken lines-open symbols) as functions of distance R between He^*(Li) and the center of mass of CH_3CN. Several directional approaches are shown with circles ($\phi=0°$, $\theta=0°$), triangles ($\phi=0°$, $\theta=60°$), squares ($\phi=0°$, $\theta=120°$), and diamonds ($\phi=0°$, $\theta=180°$). The definitions of R,θ, and ϕ are also shown.

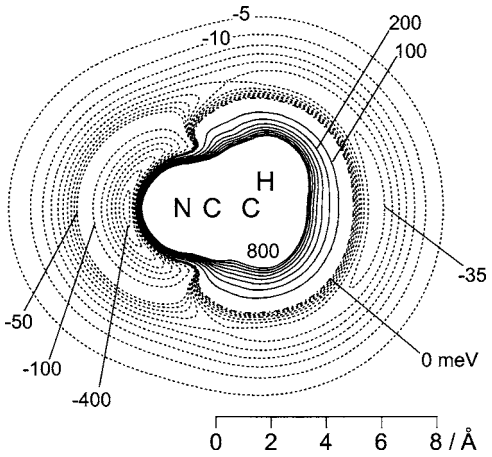

FIG. 10. Contour map of the optimized potential energy surface V_{OE} for $CH_3CN+He^*(2\,^3S)$ system drawn in the σ_v vertical plane, which includes one of the CH bonds in the methyl group ($\phi=0°$). Positive and negative values of the potential energy are shown with solid lines and dotted lines, respectively. The energy spacing of the contour lines for negative values is 50 meV for the energy range from −400 to −50 meV, and 5 meV for the energy range from −50 to 0 meV, respectively. In the case of positive values, the energy spacing is 100 meV for the energy range from 0 to 800 meV.

CH bonds in the methyl group ($-CH_3$). The above consideration on CEDPICS for $A(^2A_1)$ state can be confirmed by the optimized potential energy curve (filled circles in Fig. 9) and surface (Fig. 10), where a deep attractive well with a depth of 423 meV (ca. 10 kcal/mol) lies in the N-atom side along the C_{3v} axis (CCN axis). Table III shows the obtained potential well depth $D_{e(N)}$ in the N-atom region and its geometrical positions of $R_{e(N)}, \theta_{e(N)}$, and $\phi_{e(N)}$. It can also be reasonable that the negative collision energy dependence is obtained for $X(^2E)$ ionic state [the observed slope parameter $m=-0.41$ (E_c: 20–50 meV), −0.34 (E_c: 50–100 meV), and −0.29 (E_c: 100–330 meV)], since the $2e(\pi_{CN})$ orbital assigned to the $X(^2E)$ state has a large amount of electron density at the widely extended attractive interaction region around CN group, as can be seen in Fig. 10.

TABLE III. Optimized parameters of the exponent ζ and the coefficients C_i in Eqs. (6) and (7) for potential corrections, obtained potential-well depths $D_{e(N)}$ around the N atom, $D_{e(C)}$ around the methyl group ($-CH_3$), and their geometrical positions of $[R_{e(N)}, \theta_{e(N)}, \phi_{e(N)}$, and $R_{e(C)}, \theta_{e(C)}, \phi_{e(C)}]$ for the system of $CH_3CN+He^*(2\,^3S)$.

ζ (bohr^{-1})	0.562
C_6(meV)	4
C_5(meV)	373
C_4(meV)	1073
C_3(meV)	328
C_2(meV)	−3811
C_1(meV)	249
$D_{e(N)}$(meV)	423
$R_{e(N)}$(Å)[a]	3.20
$\theta_{e(N)}$(°)[a]	0.0
$\phi_{e(N)}$(°)[a]	0.0
$D_{e(C)}$(meV)	38
$R_{e(C)}$(Å)[a]	5.80
$\theta_{e(C)}$(°)[a]	180.0
$\phi_{e(C)}$(°)[a]	0.0

[a]The definitions of R, θ, and ϕ as can be seen in Fig. 9.

On the other hand, in the case of the ionic states of $B(^2E)$ and $C(^2A_1)$ which correspond to ionization from $1e(\sigma_{CH})$ and $6a_1(\sigma_{CC})$ MOs, respectively, curved structures with a minimum of the ionization cross section were clearly observed in CEDPICS (see Fig. 8 and Table II). It should be noted that the present theoretical calculation can account for the above feature in the observed CEDPICS for $B(^2E)$ and $C(^2A_1)$ states. In the higher collision energy region, each CEDPICS shows a positive collision energy dependence [the observed slope parameter $m=+0.32$ (E_c: 100–330 meV) for $B(^2E)$ state and +0.20 (E_c: 150–330 meV) for $C(^2A_1)$ state]. Apparently, these correspond to the region (II) in Fig. 6; as opposed to situations of the attractive interaction, in the case that repulsive interaction governs collisional ionization, ionization cross sections are expected to be larger with the increase of the collision energy, because a faster He^* atom can reach the reactive region against the repulsive wall, which results in a large overlap between relevant orbitals than a slower He^* atom.[18] Therefore, the observed positive CEDPICS in the higher E_c range for $B(^2E)$ and $C(^2A_1)$ states indicates the repulsive interaction around the H-atom and C-atom regions, respectively, where the corresponding MOs [$1e(\sigma_{CH})$ for $B(^2E)$ state and $6a_1(\sigma_{CC})$ for $C(^2A_1)$ state] have a large amount of electron density. These considerations can be supported by the optimized potential energy curves (Fig. 9) and surface (Fig. 10), where repulsive interaction around the methyl group ($-CH_3$) is expected to be dominant at higher collision energies. This has also been confirmed in the previous experimental and theoretical studies in the collision energy region of 80–300 meV.[44,46] In the lower collision energy region ($E_c<50$ meV), however, the negative collision energy dependence was observed for both $B(^2E)$ and $C(^2A_1)$ states [the observed slope parameter $m=-0.41$ for $B(^2E)$ state and −0.54 for $C(^2A_1)$ state in the collision energy range from 20 to 50 meV]. In Sec. IV E, these features have been discussed in detail.

E. Collisional ionization in producing B(^2E) and C($^2A_1$) ionic states at low collision energies

First, we focus on the CEDPICS for $B(^2E)$ ionic state. Judging from the optimized potential energy surface in Fig. 10, it is suggested that the observed negative CEDPICS for $B(^2E)$ state for CH_3CN^+ in the lower E_c range should be related to a weak attractive interaction around the H-atom region of CH_3 group, where a shallow attractive potential has been found (the well depth at the H-atom region is ca. −35 meV). In other words, at the low collision energies, the collisional ionization into the $B(^2E)$ ionic state is mainly governed by the weak attractive interaction around CH_3 group.

It is interesting that in the previous experimental work on the system of $C_2H_2+He^*(2\,^3S)$ in the collision energy range from 20 to 360 meV,[48] a similar curved structure with respect to the present CEDPICS for $B(^2E)$ ionic state of

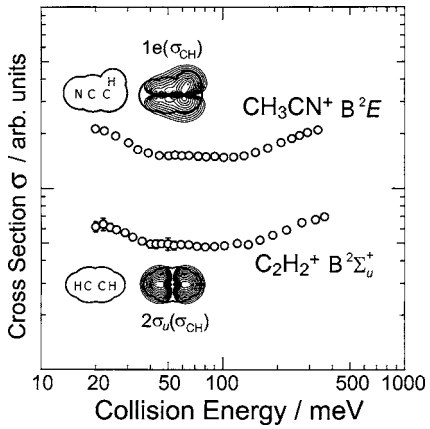

FIG. 11. Comparison of the observed CEDPICS for $B(^2E)$ ionic state of CH_3CN^+ with that for $B\ ^2\Sigma_u^+$ ionic state of $C_2H_2^+$. (Ref. 48) The contour maps of the electron density distribution of $1e(\sigma_{CH})$ MO corresponding to $B(^2E)$ ionic state of CH_3CN^+ and $2\sigma_u(\sigma_{CH})$ MO corresponding to $B\ ^2\Sigma_u^+$ ionic state of $C_2H_2^+$ are also shown.

CH_3CN^+ has been observed for CEDPICS for $A\ ^2\Sigma_g^+$ and $B\ ^2\Sigma_u^+$ ionic states of $C_2H_2^+$.[48] Figure 11 compares the observed CEDPICS of $B(^2E)$ state of CH_3CN^+ with that of $B\ ^2\Sigma_u^+$ state of $C_2H_2^+$. (The CEDPICS of $A\ ^2\Sigma_g^+$ state shows almost the same feature as that of $B\ ^2\Sigma_u^+$ state.) Here, it should be noted that the ionic state of $B\ ^2\Sigma_u^+$ for $C_2H_2^+$ corresponds to the ionization from $2\sigma_u$ MO with a σ_{CH} character, which is the same in the case of $B(^2E)$ state for CH_3CN^+ [corresponding MO is $1e(\sigma_{CH})$]. As can be seen in Fig. 11, it is obvious that both CEDPICSs have a minimum of the ionization cross section in the collision energy range from 50 to 100 meV. It has been concluded in the case of $C_2H_2 + He^*(2\ ^3S)$ system[48] that the negative CEDPICS in the lower E_c region indicates a weak attractive interaction in the H-atom region of C_2H_2 molecule (the well depth was estimated to be ca. 40 meV in a previous study).[41] This fact can support the above considerations about the observed negative collision energy dependence for $B(^2E)$ ionic state of CH_3CN^+ in the lower E_c range from 20 to 50 meV. In conclusion, the observed curved structure is connected with the transition from the region (II) to the region (I) with the decrease of the collision energy in Fig. 6.

In the case of $C(^2A_1)$ state of CH_3CN^+, however, the much larger negative value of the observed slope parameter [$m=-0.54$ (E_c: 20–50 meV) than that of $B(^2E)$ ionic state ($m=-0.41$ in the same E_c region)] cannot be related to a weak attractive interaction around the methyl group ($-CH_3$), since the magnitude of the weak attractive potential well in the H-atom region (−35 meV) is almost equal to that in the C-atom region of CH_3 group (−38 meV), as can be seen in Figs. 9 and 10. In fact, a minimum of the ionization cross section around 200 meV in the CEDPICS for $C(^2A_1)$ state was found in a previous study (E_c: 80–300 meV).[44] Classical trajectory calculations on the *ab initio* Li model potential have suggested that the observed curved structure in the $C(^2A_1)$ state should be ascribed to a change of the most reactive region from the C-atom side of CH_3 group to the N-atom side of CN group with decreasing collision energy.[44,46] From the contour map of the electron density distribution of $6a_1(\sigma_{CC})$ MO corresponding to $C(^2A_1)$ state in Figs. 7 and 8, it is apparently found that the $6a_1(\sigma_{CC})$ MO has a little but certain electron densities at the N-atom region of CN group, where the deep attractive well (−423 meV) lies, as can be seen in Figs. 9 and 10. Thus, in the lower E_c region, it should be favorable for producing $C(^2A_1)$ state when He^* metastable atoms attack to the N-atom side. This consideration is supported by the present experimental results that the observed negative slope parameter in CEDPICS for $C(^2A_1)$ state [$m=-0.54$ (E_c: 20–50 meV)] has the same value as that of $A(^2A_1)$ state, as can be seen in Table II. On the other hand, as collision energy increases, He^* metastable atoms can easily reach the reactive region of the methyl group ($-CH_3$). Therefore, ionization around the CH_3 group becomes preferred in the higher collision energy region, since $6a_1(\sigma_{CC})$ MO has much larger electron density in the C-atom region of the CH_3 group in comparison with the N-atom region of the CN group.

F. Characteristic feature of optimized potential parameters and stereospecific attractive well around the methyl group

The optimized potential parameters of C_i and ζ for the correction of Li model potential V_0 in Eqs. (6) and (7) are listed in Table III. Here, the physical meanings of the corrections for the anisotropic interaction potential energy surface between CH_3CN and $He^*(2\ ^3S)$ are discussed in terms of the above-optimized parameters.

The optimized value of 0.562 $bohr^{-1}$ of the exponent ζ in Eq. (7) is found to be very close to the exponent of the $2s$ orbital of He^* atom (0.575 $bohr^{-1}$) determined by Slater's rule for the electronic configuration $1s^12s^1$ of a He atom. This indicates that the most relevant orbital to the corrections is the valence $2s$ orbital and not the inner $1s$ orbital in a He^* atom. Moreover, this is consistent with the approximation replacing a $He^*(2\ ^3S)$ metastable atom by a $Li(2\ ^2S)$ atom neglecting the effects of inner orbitals, which is based on the assumption that the outer electron mainly governs the interactions as mentioned in Sec. III. Although general trends in optimized C_i parameters were discussed previously,[41] roles of C_i parameters in potential corrections can be summarized as follows.

(1) In the occupied MOs, the coefficients except for C_2 are positive. This feature means that contributions of C_1, C_3, and C_4 supplement $2s$-$2p$ hybridization effects,[18,28,74,75] which are underestimated in the Li model potential since the energy gap between $2s$ and $2p$ orbitals of $He^*(2\ ^3S)$ (1.114 eV) is much smaller than that of $Li(2\ ^2S)$ (1.848 eV). Although the large negative contribution of C_2 coefficient is rather puzzling, it may be caused by a subtle balance of many factors in evaluating such a highly anisotropic interaction as the present system.

(2) The coefficient C_5 [lowest unoccupied molecular orbital (LUMO)] shows a relatively large positive value. This indicates that the contribution of the coefficient C_5 supplements a charge-transfer (CT) interaction effect leading to $M^{\delta-}A^{*\delta+}$ (Refs. 76–78) in the correction of tr

TABLE IV. The relative ratio for the optimized $K^{(i)}$ parameters associated with the ionization widths for producing respective ionic states in Eq. (8).

Ionic state	Relative ratio of $K^{(i)}$	Ionization potential (eV)[a]
$X(^2E)$	1.00	12.20
$A(^2A_1)$	1.43	13.13
$B(^2E)$	2.47	15.13
$C(^2A_1)$	3.30	17.58[b]

[a]Adiabatic ionization potentials taken from Refs. 72 and 73.
[b]Vertical ionization potential.

Li model potential V_0. Since the ionization potential of Li($2\,^2S$) (5.392 eV) is larger than that of $He^*(2\,^3S)$ (4.768 eV), the energy level of the $2s$ electron of $He^*(2\,^3S)$ is much higher in comparison with that of Li($2\,^2S$). Thus, the CT interaction is much more important in the case of $He^*(2\,^3S)$ because of the smaller energy gap between the $2s$ and LUMO for $He^*(2\,^3S)$. It should be noted that LUMO $8a_1$ has a large electron distribution around the methyl group ($-CH_3$), as can be seen in Fig. 2. In fact, it has been found in the present study that a shallow attractive well with a depth of 38 meV lies at a distance of 5.80 Å from the center of mass of CH_3CN in the C-atom side along the C_{3v} axis. Table III summarizes the attractive well depth $D_{e(C)}$ around the methyl group and its geometrical positions $R_{e(C)}$, $\theta_{e(C)}$, and $\phi_{e(C)}$. From the above considerations, a weak attractive interaction around the methyl group is mainly related to the orbital interaction between LUMO $8a_1$ of CH_3CN and $2s$ atomic orbital of $He^*(2\,^3S)$ metastable atom. It is worth mentioning that a similar stereospecific attractive potential well around the methyl group has been calculated by semiempirical methods for the interaction system of CH_3Cl+Ne^*;[32,78] the CT interaction effect leading to $CH_3Cl^{\delta-}Ne^{*\delta+}$ has a substantial contribution to the attractive potential well around the methyl group, since the LUMO of CH_3Cl has a C–Cl σ-antibonding character.[78]

The present estimation of the ionization width $\Gamma^{(i)}$ was found to be satisfactory in accounting for the branching ratio of the observed CEDPICS, as can be seen in Fig. 8. Table IV lists the relative ratio between the optimized $K^{(i)}$ parameters associated with the ionization width for producing respective ionic states $\Gamma^{(i)}$ in Eq. (8) and their ionization potentials. Although the validity of the present approximation of $\Gamma^{(i)}$ was discussed previously,[41–44] here we should briefly remark on $K^{(i)}$ parameters. In Table IV, it should be noted that the larger the IP of the ionic states, the larger the corresponding value of $K^{(i)}$. This tendency can be found in the previous works by using the overlap approximation for $\Gamma^{(i)}$,[41–44] and may be partly due to a factor of $E_e^{-1/2}$ in a formula of the ionization width.[79]

V. CONCLUSION

A discharge nozzle source with a liquid-N_2 circulator for producing low velocity $He^*(2\,^3S)$ metastable beams has been developed in order to obtain the state-resolved collision energy dependence of Penning ionization cross sections in a low collision energy range from 20 to 80 meV. The properties of the metastable atomic beams were investigated on the basis of the shifted Maxwellian velocity distribution. It is found that by controlling the discharge condition, we have been able to measure the collision energy dependence of *partial* ionization cross sections (CEDPICS) for molecular targets with various ionic states in the energy range from 20 to 350 meV.

The anisotropic potential energy surface for the system of $CH_3CN+He^*(2\,^3S)$ has been obtained starting from an *ab initio* model potential via an optimization procedure based on classical trajectory calculations for the observed CEDPICS. The overlap expansion method for improving the model potential has enabled us to understand the physical meaning of potential corrections as well as to construct highly anisotropic intermolecular potentials.

A dominant attractive well depth was found to be 423 meV (ca. 10 kcal/mol) in the N-atom side along the CCN axis. In addition, a weak attractive well (ca. 0.9 kcal/mol) surrounding the methyl group ($-CH_3$) has been found for the first time. It is found that the weak attractive potential surrounding the methyl group ($-CH_3$) plays a dominant role in collisional ionization into $B(^2E)$ ionic state at lower collision energies. From the analysis of the optimized parameters for potential corrections, it is concluded that this shallow attractive well is related to the orbital interaction between LUMO $8a_1$ of CH_3CN and $2s$ atomic orbital of $He^*(2\,^3S)$ metastable atom.

ACKNOWLEDGMENTS

The present work was supported by a Grant in Aid for Scientific Research from the Ministry of Education, Culture, Sports, Science, and Technology (MEXT). Three of the authors (T.H., M.Y., and S.M.) are supported by the Research Fellowship of the Japan Society for the Promotion of Science for Young Scientists.

[1] F. M. Penning, Naturwiss. **15**, 818 (1927).
[2] H. Hotop and A. Niehaus, Z. Phys. **228**, 68 (1969).
[3] V. Čermák, J. Chem. Phys. **44**, 3781 (1966).
[4] A. Niehaus, Adv. Chem. Phys. **45**, 399 (1981).
[5] A. J. Yencha, in *Electron Spectroscopy: Theory, Techniques and Applications*, edited by C. R. Brundle and A. D. Baker (Academic, New York, 1984), Vol. 5.
[6] K. Ohno, H. Mutoh, and Y. Harada, J. Am. Chem. Soc. **105**, 4555 (1983).
[7] K. Ohno, S. Matsumoto, and Y. Harada, J. Chem. Phys. **81**, 4447 (1984).
[8] K. Ohno and Y. Harada, in *Theoretical Models of Chemical Bonding*, edited by Z. B. Maksić (Springer, Berlin, 1991), pt. 3, p. 199.
[9] S. Y. Tang, A. B. Marcus, and E. E. Muschlitz, Jr., J. Chem. Phys. **56**, 566 (1972).
[10] E. Illenberger and A. Niehaus, Z. Phys. B **20**, 33 (1975).
[11] A. Pesnelle, G. Watel, and C. Manus, J. Chem. Phys. **62**, 3590 (1975).
[12] M. R. Woodard, R. C. Sharp, M. Seely, and E. E. Muschlitz, Jr., J. Chem. Phys. **69**, 2978 (1978).
[13] R. M. Martin and T. P. Parr, J. Chem. Phys. **70**, 2220 (1979).
[14] T. P. Parr, D. M. Parr, and R. M. Martin, J. Chem. Phys. **76**, 316 (1982).
[15] L. Appolloni, B. Brunetti, J. Hermanussen, F. Vecchiocattivi, and G. G. Volpi, J. Chem. Phys. **87**, 3804 (1987).
[16] R. Feltgen, H. Ferkel, R. K. B. Helbing, A. Lindinger, D. Pikorz, and H. Vehmeyer, J. Chem. Phys. **111**, 7298 (1999).
[17] K. Mitsuke, T. Takami, and K. Ohno, J. Chem. Phys. **91**, 1618 (1989).

[18] K. Ohno, T. Takami, K. Mitsuke, and T. Ishida, J. Chem. Phys. **94**, 2675 (1991).
[19] T. Takami, K. Mitsuke, and K. Ohno, J. Chem. Phys. **95**, 918 (1991).
[20] D. C. Dunlavy, D. W. Martin, and P. E. Siska, J. Chem. Phys. **93**, 5347 (1990).
[21] P. E. Siska, Rev. Mod. Phys. **65**, 337 (1993).
[22] D. C. Dunlavy, D. W. Martin, and P. E. Siska, J. Phys. Chem. **100**, 21 (1996).
[23] F. Biondini, B. G. Brunetti, P. Candori, F. De Angelis, S. Falcinelli, F. Tarantelli, M. M. Teixidor, F. Pirani, and F. Vecchiocattivi, J. Chem. Phys. **122**, 164307 (2005).
[24] K. Ohno, H. Yamakado, T. Ogawa, and Y. Yamata, J. Chem. Phys. **105**, 7536 (1996).
[25] N. Kishimoto, M. Furuhashi, and K. Ohno, J. Electron Spectrosc. Relat. Phenom. **88–91**, 143 (1998).
[26] H. Nakamura, J. Phys. Soc. Jpn. **26**, 1473 (1969).
[27] W. H. Miller, J. Chem. Phys. **52**, 3563 (1970).
[28] J. S. Cohen and N. F. Lane, J. Chem. Phys. **66**, 586 (1977).
[29] A. P. Hickman, A. D. Isaacson, and W. H. Miller, J. Chem. Phys. **66**, 1492 (1977).
[30] T. Ishida, Chem. Phys. Lett. **191**, 1 (1992).
[31] T. Ishida and K. Horime, J. Chem. Phys. **105**, 5380 (1996).
[32] M. Albertí, J. M. Lucas, B. Brunetti, F. Pirani, M. Stramaccia, M. Rosi, and F. Vecchiocattivi, J. Phys. Chem. A **104**, 1405 (2000).
[33] F. Biondini, B. G. Brunetti, P. Candori, F. De Angelis, S. Falcinelli, F. Tarantelli, F. Pirani, and F. Vecchiocattivi, J. Chem. Phys. **122**, 164308 (2005).
[34] F. A. U. Thiel, L. Thiel, A. J. Yencha, M.-W. Ruf, W. Meyer, and H. Hotop, J. Phys. B **37**, 3691 (2004).
[35] L. Thiel, H. Hotop, and W. Meyer, J. Chem. Phys. **122**, 184309 (2005).
[36] E. W. Rothe, R. H. Neynaber, and S. Trujillo, J. Chem. Phys. **42**, 3310 (1965).
[37] H. Hotop, Radiat. Res. **59**, 379 (1974).
[38] H. Haberland, Y. T. Lee, and P. E. Siska, Adv. Chem. Phys. **45**, 487 (1981).
[39] H. Hotop, T. E. Roth, M.-W. Ruf, and A. J. Yencha, Theor. Chem. Acc. **100**, 36 (1998).
[40] T. Ogawa and K. Ohno, J. Chem. Phys. **110**, 3773 (1999).
[41] S. Maeda, M. Yamazaki, N. Kishimoto, and K. Ohno, J. Chem. Phys. **120**, 781 (2004).
[42] K. Ohno, M. Yamazaki, S. Maeda, and N. Kishimoto, J. Electron Spectrosc. Relat. Phenom. **142**, 283 (2005).
[43] M. Yamazaki, S. Maeda, N. Kishimoto, and K. Ohno, J. Chem. Phys. **122**, 044303 (2005).
[44] M. Yamazaki, S. Maeda, N. Kishimoto, and K. Ohno, J. Chem. Phys. **117**, 5707 (2002).
[45] T. Pasinszki, H. Yamakado, and K. Ohno, J. Phys. Chem. **99**, 14678 (1995).
[46] T. Ogawa and K. Ohno, J. Phys. Chem. A **103**, 9925 (1999).
[47] Y. Yamakita, H. Tanaka, R. Maruyama, H. Yamakado, F. Misaizu, and K. Ohno, Rev. Sci. Instrum. **71**, 3042 (2000).
[48] T. Horio, T. Hatamoto, N. Kishimoto, and K. Ohno, Chem. Phys. Lett. **397**, 242 (2004).
[49] T. Hsu and J. L. Hirshfield, Rev. Sci. Instrum. **47**, 236 (1976).
[50] G. Beamson, H. Q. Porter, and D. W. Turner, J. Phys. E **13**, 64 (1980).
[51] G. Beamson, H. Q. Porter, and D. W. Turner, Nature (London) **290**, 556 (1981).
[52] S. F. Boys and F. Bernardi, Mol. Phys. **19**, 553 (1970).
[53] M. J. Frisch, G. W. Trucks, H. B. Schlegel *et al.*, GAUSSIAN 94, Revision C.3, Gaussian, Inc., Pittsburgh, PA, 1995.
[54] K. Ohshimo, H. Tsunoyama, Y. Yamakita, F. Misaizu, and K. Ohno, Chem. Phys. Lett. **301**, 356 (1999).
[55] J. B. Anderson and J. B. Fenn, Phys. Fluids **8**, 780 (1965).
[56] A. Bard, K. K. Berggren, J. L. Wilbur, J. D. Gillaspy, S. L. Rolston, J. J. McClelland, W. D. Phillips, M. Prentiss, and G. M. Whitesides, J. Vac. Sci. Technol. B **15**, 1805 (1997).
[57] X. Ju, M. Kurahashi, T. Suzuki, and Y. Yamauchi, Thin Solid Films **438–439**, 128 (2003).
[58] A. Robert, O. Sirjean, A. Browaeys, J. Poupard, S. Nowak, D. Boiron, C. I. Westbrook, and A. Aspect, Science **292**, 461 (2001).
[59] N. Herschbach, P. J. J. Tol, W. Vassen, W. Hogervorst, G. Woestenenk, J. W. Thomsen, P. van der Straten, and A. Niehaus, Phys. Rev. Lett. **84**, 1874 (2000).
[60] M. Doery, M. Widmer, J. Bellanca, E. Vredenbregt, T. Bergeman, and H. Metcalf, Phys. Rev. Lett. **72**, 2546 (1994).
[61] W. Rooijakkers, W. Hogervorst, and W. Vassen, Opt. Commun. **123**, 321 (1996).
[62] H. C. Mastwijk, M. van Rijnbach, J. W. Thomsen, P. van der Straten, and A. Niehaus, Eur. Phys. J. D **4**, 131 (1998).
[63] G. R. Woestenenk, J. W. Thomsen, M. van Rijnbach, P. van der Straten, and A. Niehaus, Rev. Sci. Instrum. **72**, 3842 (2001).
[64] W. Lu, M. D. Hoogerland, D. Milic, K. G. H. Baldwin, and S. J. Buckman, Rev. Sci. Instrum. **72**, 2558 (2001).
[65] J. A. Swansson, K. G. H. Baldwin, M. D. Hoogerland, A. G. Truscott, and S. J. Buckman, Appl. Phys. B: Lasers Opt. **79**, 485 (2004).
[66] M. DeKieviet, M. Dürr, S. Epp, F. Lang, and M. Theis, Rev. Sci. Instrum. **75**, 345 (2004).
[67] D. W. Fahey, W. F. Parks, and L. D. Schearer, J. Phys. E **13**, 381 (1980).
[68] D. R. Miller, in *Atomic and Molecular Beam Methods*, edited by G. Scoles (Oxford University Press, New York, 1988), Vol. 1, Chap. 2.
[69] R. E. Olson, Phys. Rev. A **6**, 1031 (1972).
[70] N. C. Handy, M. T. Marron, and H. J. Silverstone, Phys. Rev. **180**, 45 (1969).
[71] M. M. Morrell, R. G. Parr, and M. Levy, J. Chem. Phys. **62**, 549 (1975).
[72] K. Kimura, S. Katsumata, Y. Achiba, T. Yamazaki, and S. Iwata, *Handbook of He I Photoelectron Spectra of Fundamental Organic Molecules* (Japan Scientific, Tokyo, 1981).
[73] M. Gochel-Dupuis, J. Delwiche, M.-J. Hubin-Franskin, and J. E. Collin, Chem. Phys. Lett. **193**, 41 (1992).
[74] A. D. Isaacson, A. P. Hickman, and W. H. Miller, J. Chem. Phys. **67**, 370 (1977).
[75] P. E. Siska, J. Chem. Phys. **71**, 3942 (1979).
[76] J. L. Magee, J. Chem. Phys. **8**, 687 (1940).
[77] V. Aquilanti, D. Cappelletti, and F. Pirani, Chem. Phys. Lett. **271**, 216 (1997).
[78] B. Brunetti, P. Candori, J. De Andres, F. Pirani, M. Rosi, S. Falcinelli, and F. Vecchiocattivi, J. Phys. Chem. A **101**, 7505 (1997).
[79] W. H. Miller, C. A. Slocomb, and H. F. Schaefer III, J. Chem. Phys. **56**, 1347 (1972).